Journal of Environmental Management 349 (2024) 119366

Contents lists available at ScienceDirect

Journal of Environmental Management

journal homepage: www.elsevier.com/locate/jenvman

Research article

Integrated methodology to link geochemical and geophysical-lab data in a geophysical investigation of a slag heap for resource quantification

Itzel Isunza Manrique [a,*], Thomas Hermans [b], David Caterina [a], Damien Jougnot [c], Benoît Mignon [d], Antoine Masse [d], Frédéric Nguyen [a]

[a] Urban and Environmental Engineering, University of Liege, Quartier Polytech 1, Allée de la Découverte 9 – B52, 4000, Liege, Belgium
[b] Department of Geology (WE13), Ghent University, Campus Sterre, S8, Krijgslaan 281, B-9000, Gent, Belgium
[c] UMR 7619 METIS, Sorbonne Université, 4 place Jussieu, 75252, Paris, France
[d] Centre Technologique International de la Terre et de la Pierre, 55 Chaussée d'Antoing, Tournai, 7500, Belgium

ARTICLE INFO

Handling Editor: Prof Raf Dewil

Keywords:
Metallurgical residues
Resource-recovery
Geochemical analysis
Geophysics
Electrical resistivity tomography
Induced polarization

ABSTRACT

The increasing need to find alternative stocks of critical raw materials drives to revisit the residues generated during the former production of mineral and metallic raw materials. Geophysical methods contribute to the sustainable characterization of metallurgical residues inferring on their composition, zonation and volume(s) estimation. Nevertheless, more quantitative approaches are needed to link geochemical or mineralogical analyses with the geophysical data. In this contribution, we describe a methodology that integrates geochemical and geophysical laboratory measurements to interpret geophysical field data solving a classification problem. The final aim is to estimate volume(s) of different types of materials to assess the potential resource recovery. We illustrate this methodology with a slag heap composed of residues from a former iron and steel factory. First, we carried out a 3D field acquisition using electrical resistivity tomography (ERT) and induced polarization (IP), based on which, a sampling survey was designed. We conducted laboratory measurements of ERT, IP, spectral induced polarization (SIP), and X-ray fluorescence analysis, based on which, 4 groups of different chemical composition were identified. Then we carried out a 3D probabilistic classification of the field data, based on 2D kernel density estimators (for each group) fitted to the inverted data collocated with the samples. The estimated volumes based on the classification model were: 4.17×10^3 m^3 ± 12 %, 1.888×10^5 m^3 ± 12 %, 59.4×10^3 m^3 ± 19 %, and 2.30×10^4 m^3 ± 21% for the groups ordered with an increasing metallic content. The uncertainty ranges were derived from comparing the volumes with and without considering the probabilities associated to the classification. We found that a representative sampling and the definition of the KDE bandwidths are defining elements in the classification and ultimately the estimation of volumes. This methodology is suitable to quantitatively interpret geophysical data in terms of the geochemical composition of the materials, integrating uncertainties both in the classification and the estimation of volumes. Furthermore, several crucial elements in the investigation of metallurgical residues could be applied in a real case study, e.g., geophysical field acquisition, sampling and lab measurements.

1. Introduction

Former mining and metallurgical activities are often associated with the long-term contamination in soils, lakes, and estuarine sediments among others, which may be detectable even centuries after the end of activities on site (Martínez Cortizas et al., 2016; Asare and Afriyie, 2021). Simultaneously, the recent need of raw materials, metals and minerals, emphasizes the challenges faced by the mining industry (Žibret et al., 2020) and highlights the need to explore alternative material sources.

Past mining and metallurgical sites offer an opportunity to mitigate this situation if we are able to assess the potential recovery of buried mine or metallurgical materials treated as waste, since mineral processing and metallurgical treatments were not as efficient as they are nowadays. What was considered as metalliferous wastes (dusts, slags, tailings, etc.) can therefore still contain valuable materials. Primarily,

* Corresponding author.
E-mail address: iisunza@uliege.be (I. Isunza Manrique).

https://doi.org/10.1016/j.jenvman.2023.119366
Received 9 June 2023; Received in revised form 23 September 2023; Accepted 14 October 2023
Available online 27 October 2023

these residues may still contain valuable ferrous and non-ferrous metals, rare earth elements and other critical raw materials (Sethurajan et al., 2018) and ultimately, they could be reprocessed and used in the construction industry (Machiels et al., 2022) as aggregates or for cement. Therefore, remediation strategies that aim to prevent or reduce the release of pollutants into the environment and reduce waste volumes can also be targeted to enhance secondary resource recovery (Izydorczyk et al., 2021; Vareda et al., 2019). To exploit such resources efficiently, it is crucial to have in-depth knowledge on the available quantities, composition, heterogeneity, and physical and chemical properties (Asare and Afriyie, 2021; Dino et al., 2021; Žibret et al., 2020).

Geophysical methods have proven useful to characterize metallurgical wastes and associated contamination. For example, electromagnetic induction (EMI) and electrical resistivity tomography (ERT) have been used to identify waste dumps from lead and silver production and to estimate volumes (Martin et al., 2020; Mendecki et al., 2020), qualitatively validated with optimized sampling (e.g., boreholes, pits). Other types of slags may not be easily detected using only ERT as indicated in Florsch et al. (2011, 2012), who used additionally magnetometry and induced polarization (IP) to estimate the volume of a slag heap from iron and steel production. The volume was estimated using a laboratory-derived linear relationship between the chargeability and the slag concentration.

Note that comprehensive characterizations such as mineral or metallurgical zonation, may require integrated approaches to link geophysical measurements in the field and/or in the laboratory with optimized sampling and metallurgical or geochemical analysis (Van De Vijver et al., 2021). For example, Lévy et al. (2019) qualitatively compare inverted spectral parameters from time domain 2D IP-ERT field data with in situ borehole measurements, mineral distribution analysis and SIP laboratory measurements to study the lithology and mineral composition of a geothermal area. The methodology allowed to discriminate between zones rich in pyrite from those zones with iron oxides (magnetite-rich). Johansson et al. (2020) compared inverted SIP parameters from time-domain IP field data with SIP from laboratory measurements from a 50 m long rock core drilled along one field profile. The study was carried out on a limestone succession and the solid parts of the core were used for the analysis of physicochemical characteristics of the rocks in the laboratory, based on which, the geophysical data were interpreted. The results showed that the inverted parameters of the field data (closer to the borehole) were comparable to the SIP lab measurements despite the differences in measurements techniques and scale.

More quantitative techniques to ultimately interpret field data considering the link between laboratory and field measurements, include data classification and machine learning algorithms. For example, Vásconez-Maza et al. (2019) predicted the distribution of chromium in an abandoned phosphogypsum pond through a classification of ERT field data. The authors used a non-linear relationship between the concentration of chromium measured in the lab and the inverted field resistivity collocated with the samples' positions. More recently, (Martin et al., 2021) investigated slags from different historical dumps derived from processing of metal ores. The authors measured SIP in the laboratory and carried out geochemical and mineralogical analyses in samples collected at maximum depths of 0.5 m. In the field, they collected two 2D SIP profiles with a limited bandwidth. Three slags grades could be identified in the laboratory and in the field based on the polarization magnitude. Additionally, the slags could be classified in five categories according to the shape of their spectra which could reflect the diversity of environmental parameters such as saturation or fluid conductivity. For machine learning applications, Zhang et al. (2023) mapped a mine tailing pong using an unmanned aerial vehicle with a hyperspectral sensor, and collected 74 soil samples in which copper and organic content were measured. A simulated annealing deep neural network was then used to predict the available copper/organic matter from the hyperspectral data.

In this contribution, we propose a quantitative approach to integrate laboratory and field measurements to perform a 3D classification within a slag heap in a probabilistic manner. The main objective is to define a zonation based on chemical composition and to estimate the volumes of different materials within the slag heap for potential resource recovery. To this aim, we followed a quantitative approach that integrates: 1) 3D ERT and IP measurements in the field, 2) a targeted sampling with samples' collection at 22 different positions in the heap, 3) laboratory measurements of ERT, IP and SIP and 4) a chemical characterization of samples through X-ray fluorescence (XRF) analysis. We used laboratory measurements and chemical analysis to identify groups of samples of different composition and properties. The identification of these clusters was supported by studying the relationships between the chemical and geophysical variables, an unsupervised clustering algorithm (hierarchical clustering), and a PCA analysis. Then, we linked the laboratory with the field measurements by fitting the resistivity and chargeability field data collocated with the sampling using 2D kernel density estimation (KDE) functions for each previously defined group. Afterwards we computed the joint conditional probabilities in the whole field domain. Lastly, we classify the 3D inverted models in terms of the groups and compute the corresponding volumes.

2. Site description

The site of Duferco – La Louvière, located in the Province of Hainaut (Belgium), is an idled factory of iron and steel production that started its activities around 1850 and officially stopped in 2013. The site evolved and reached its final infrastructure in 1981, integrating elements such as a coking plant, blast furnaces and agglomerations of by-products and raw materials in the northeast zone (see Fig. 1a). In this contribution, we study the storage of slags located in the northern zone of the site where the backfilling started around 1930's and comes from steel works and blast furnaces. In the last decades of activity, the materials of the slag heap were mostly produced from electric arc furnaces and in particular from the ladle refining furnaces. These materials are typically rich in lime and alumina. It is likely that the most recent layers in the western area of the heap contain a mixture of residues (e.g., scrap metal, wood and refractories).

3. Methodology

Fig. 2 shows the workflow of the methodology that integrates several elements which are crucial in the investigation of metallurgical residues, and that could be tested in the site of Duferco. It comprises geophysical field measurements, based on which, a targeted sampling is designed and samples are collected. Geophysical and geochemical laboratory measurements are then carried out. Then, all the lab data are studied through a statistical analysis where different groups or clusters representing distinct types of materials are identified. Finally, a probabilistic classification is conducted in the whole field data domain and the volumes of each group are estimated.

3.1. Field measurements and targeted sampling

First, we measured ERT and time-domain IP along four profiles deployed across the entire slag heap and each profile was composed of 64 stainless electrodes spaced by 2 m (see Fig. 1b, blue dots). The measurements were collected with an ABEM Terrameter LS – Guideline Geo. Data acquisition was carried out simultaneously on combinations of two profiles, with inline and crossline measurements, to obtain truly 3D information for the inversion (Van Hoorde et al., 2017). A gradient array with a "s" factor equals to 7 was used (Dahlin and Zhou, 2006) and it was complemented with a bipole-bipole acquisition. This 3D acquisition was a tradeoff between the maximization of the heap's coverage and the spatial resolution. Electrical current was injected for 2 s and the voltage decay was measured for 1.86 s after the current was switched off. Two stacks (repetition error) and a sample of reciprocal

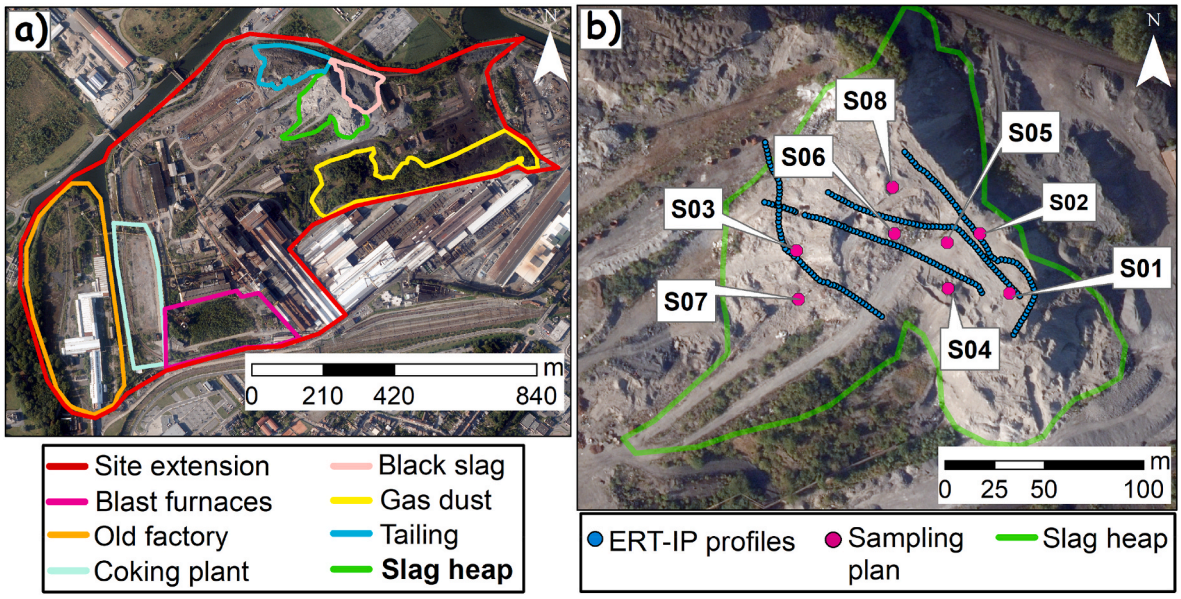

Fig. 1. a) Map of Duferco -La Louvière with the different production and agglomeration zones, b) Location of the ERT-IP acquisition profiles (blue) and sampling plan (pink) in the slag heap.

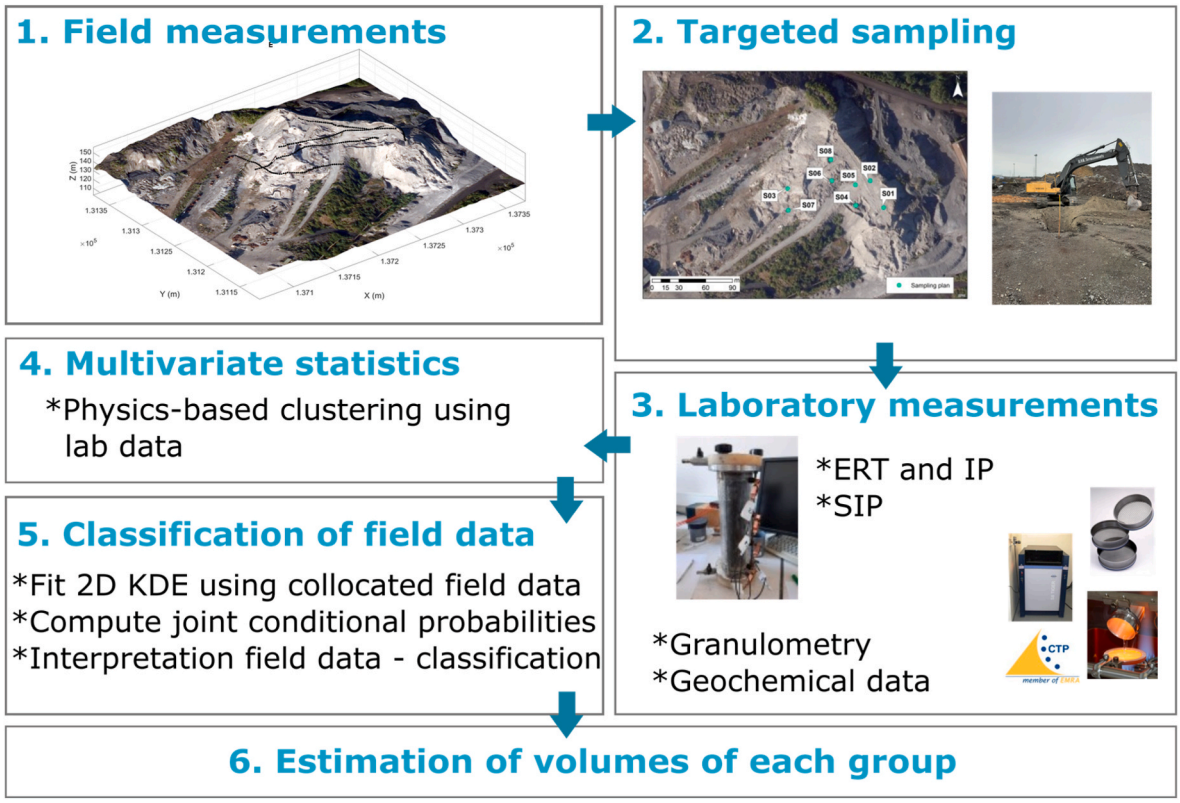

Fig. 2. Methodology integrating several steps that are crucial in the investigations of metallurgical residues. It integrates 1) geophysical field measurements based on which, 2) a targeted sampling is designed and samples are collected. 3) Geophysical and geochemical laboratory measurements are then carried out. Then, 4) all the lab data are studied through a statistical analysis where different groups representing distinct types of materials are identified. Finally, 6) a probabilistic classification is conducted in the whole field data domain and 7) the volumes of each group are estimated.

measurements were collected to assess data quality. Then, data were filtered removing measurements with a repetition error greater than 5 % in resistance. The error model from reciprocal measurements was to 0.029 Ω and 2.27 % for the absolute and relative errors (Slater et al., 2000). The data were inverted with BERT (Günther et al., 2006) using a robust constraint on the data and blocky constraint on the model to derive 3D models of electrical resistivity and chargeability while respecting the noise level ($\chi^2 = 1$).

Secondly, we designed a targeted sampling based on the contrasts observed in the ERT and IP models, i.e., targeting zones of low,

intermediate and high resistivity/chargeability values and covering most of the (shallow) observed contrasts in the inverted models. Samples were collected at 8 locations on the heap at depths of 1, 3 and 5 m (see locations in Fig. 1b, pink dots). During the sampling we took approximately 10–15 kg of material in buckets that were sealed and stored in a cold environment. The maximum depth of excavation was limited by the terrain stability, the hardness of the soil and the machine used. Additionally, heterogeneous waste at one location impeded the collection of material at two depths, therefore in this study we use 22 samples in total. As will be explained in the results, based on the inverted models, we assume that the 22 samples taken at different positions (x, y, z) captures the variations of physical and chemical properties in the slag heap.

The identifiers we use to refer to the samples indicate its location followed by an underscore and the depth of collection, i.e., S01_3 is the sample located at S01 collected at 3 m.

3.2. Laboratory measurements

3.2.1. Geophysical data

The laboratory measurements were carried out using the samples as they were collected in the field, i.e., no re-saturation, as the aim was to measure their properties in the same conditions as in the field. Geophysical measurements of resistivity (ρ_{lab}) and chargeability (m_{lab}) were collected with an ABEM Terrameter LS – Guideline Geo, using columns of 1.5 dm^3 (0.08 m diameter × 0.3 m length, see Fig. A Supp. Mat.). The potential electrodes are made of brass and the current transmission porous plates, which are in the bases of the cylinder, are made of bronze.

First, the geometric factor KG was estimated based on the resistance measured when the column was filled with water at a known conductivity ($KG = 0.045\ m^{-1}$). We then filled the columns with 1–1.5 kg of the material of each sample. First, we measured the electrical resistance and the time-domain chargeability using 4 electrodes with a Wenner array. Electrical current was injected for 2 s and voltage decay was measured for 1.86 s after switching the current off, as for the field data. Two stacks were collected to have a repetition error which was <1 % in resistance for all the samples.

Then we measured SIP in the same columns using the impedance analyzer ZEL-2-SIP04-V05 (Zimmermann et al., 2008). The impedance and phase shift were measured in the range of 10 mHz–45 kHz for the reciprocal and normal setup, leading to a high phase accuracy of 0.1 mrad (below 1 kHz).

3.2.2. Granulometry and geochemical data

Geochemical analyses were conducted in the same volumes of samples as those used for the geophysical laboratory measurements. First, each sample was sieved to determine the particle size distribution, by separating and classifying the material with a series of square mesh sieves of decreasing standardized size (NF P18-260). Then, the subsamples at the different particle sizes were analyzed using X-ray fluorescence (XRF) for major elements (e.g., Fe, Si, Mn, Ca) using the S8 TIGER from Bruker. Finally, the average content over all particle sizes was computed per element for each of the 22 samples. The average content of only six elements was larger than 1 wt % for all samples: Si, Ca, Fe, Mg, Al and Mn. The elements with the largest concentrations were Si, Ca and Fe with average contents up to around 30 wt %.

XRD analyses were also carried out, however, there was an unidentifiable amorphous phase that was relatively abundant (up to 60 wt% for some samples) and which may still contain elements that cannot be quantified with this method. Note that in a pyrometallurgical operation, the slag floating on top of a molten metal bath is separated when it is still in a semi-liquid or pasty state, and as it is rapidly cooled, it may not have time to crystallize properly, resulting in amorphous phases.

3.3. Multivariate statistics

The objective of this step is to identify groups of samples with different chemical composition and simultaneously, to identify the geophysical parameters that can distinguish these groups.

We used Pearson's correlation to quantify the linearity between the geophysical and geochemical parameters. As it has been reported previously, there is a linear relationship between the chargeability and the volumetric concentration of metallic particles, observed both in numerical simulations and experimental data (Florsch et al., 2011; Qi et al., 2018; Revil et al., 2022). In addition, a linear relationship has also been observed between the resistivity and the metallic concentration of elements such as Zn, Pb, Ni and Cu (Vásconez-Maza et al., 2021). Finally, Pearson's correlation coefficient allows also to test the direction of association in the linear relationship (e.g., Das et al., 2023).

First, we studied the linear correlations between pairs of the chemical elements constituting all the samples (average content) using the python library of Pandas (Reback et al., 2020). We applied a standardization of the data by removing the mean and scaling to unit variance using scikit-learn (Pedregosa et al., 2011), and then we computed the Pearson' correlation coefficients. The standardization of the data allows to compare the variations of the different variables using the same scale. At this step we consider strong positive and negative correlations of elements as a first indicator of different types of slags.

Afterwards, we computed the pairwise Pearson' correlation coefficients between the geochemical variables and the geophysical variables measured both in the laboratory and in the field. The field measurements were obtained from the inverted resistivity and chargeability models, computing an average of the cells within a volume of dimensions 3 m × 3 m × 1.6 m centered at the positions where the samples were collected, i.e., ρ and m. The correlations were also computed using previously standardized data.

Furthermore, we studied the relation between the resistivity and the chargeability measured in the laboratory, together with the concentration of some chemical elements with which the largest correlations were observed, to identify groups or clusters of different composition. Similarly, we analyzed the scatterplots of the imaginary and real components of the conductivity measured in SIP.

Additionally, we carried out an unsupervised learning approach (hierarchical clustering) to group the samples from the lab data and compare it with the groups previously identified. Lastly, we applied PCA to support the geophysical-geochemical-based definition of groups in the principal component space, using the standardized geochemical and geophysical data. These techniques were conducted using the python library of scikit-learn (Pedregosa et al., 2011).

3.4. Classification of the field data

In the literature, we can find quantitative interpretations of inverted geophysical data integrating ground truth data and which are based on machine learning (Lysdahl et al., 2022; Moghadas and Badorreck, 2019; Whiteley et al., 2021) and exclusively on statistics or probability theory (Dewar and Knight, 2020; Hermans and Irving, 2017; Isunza Manrique et al., 2023).

Here, we used a probabilistic approach to interpret the field data in terms of the classes or groups previously identified using laboratory measurements. Similar to Isunza Manrique et al. (2023), we derive joint conditional probabilities of each identified group in the whole field range, using the volume-averaged field data ρ and m collocated with the sampling, but here, we use a different probability density function in 2D. Note that variations of resistivity are not expected to be indicators of different types of slags (Florsch et al., 2011) but potential indicators of different types of materials within the heap, while a linear relationship has been observed between the chargeability and slag concentration (Florsch et al., 2011; Qi et al., 2018).

The kernel density estimator $f_{KDE}(y)$ at a point y based on a dataset of

points x_j for $j = 1 \ldots N$ is defined as

$$f_{KDE}(y) = \sum_{j=1}^{N} K(y - x_j; h)$$

where K is the kernel and h is the bandwidth (Pedregosa et al., 2011).

First, we used 2D KDE's to model the distributions of the volume-averaged field data $x_j = (\rho, m)_j$ for each group A_i ($i = 1 \ldots 4$), using a Gaussian kernel expressed as $K \propto \exp(-x^2/2h^2)$. The bandwidth was estimated using the data-based Scott's Rule which considers the number of data and dimension, and an estimate of the standard deviation of the bivariate data distribution (Scott, 1992; Virtanen et al., 2020). Then, we estimated the KDE's functions at all the inverted resistivity values ($\boldsymbol{P}$) and chargeability values ($\boldsymbol{M}$), i.e., whole field data domain $\boldsymbol{y} = (\boldsymbol{P}, \boldsymbol{M})$, as

$$f_{KDE}(\boldsymbol{y}|A_i) = \sum_{j=1}^{N} K(\boldsymbol{y} - \boldsymbol{x}_j; h) \quad (1)$$

See Pedregosa et al. (2011). Afterwards we used Bayes' rule and computed the joint conditional probabilities $P(A_i|\boldsymbol{y})$ of each group. The prior probability values $P(A_i)$ were estimated from the number of lab samples belonging to each group.

Each grid cell of the inversion is then classified in the group having the largest joint conditional probability, while the probability itself gives an idea of the uncertainty of the classification.

3.5. Estimation of volumes

Once the inverted model is interpreted in terms of groups or classes, we estimate the volumes of each group according to the corresponding cells' mesh using the python library of PyVista (Sullivan and Kaszynski, 2019). As each cell has been classified on the basis of a joint conditional probability, groups selected as the most likely class that have low probability values can be overestimated while groups with smaller probabilities can be underestimated. To integrate this classification uncertainty into account, we estimate the volume of each group V_i by adding the volume of the corresponding cell v, weighted with the corresponding value of joint conditional probability $P(A_i|\boldsymbol{y})$ as

$$V_i = \sum_{j=1}^{n} P(A_i|\boldsymbol{y})v \quad (2)$$

See Canters (1997). Then, by comparing the probability weighted volumes with the volumes estimated without considering associated probabilities, we could derive uncertainty ranges for the volume of each group.

4. Results

4.1. Inverted ERT and IP models and sampling

The inverted models are displayed in Fig. 3 for several cross-sections along the x and y axis. These include a (normalized) cumulative sensitivity threshold ($>10^{-5.5}$) to keep only parts of models that are sufficiently well covered (Caterina et al., 2013). The sensitivity model is shown in Figure B of Supp. Mat. We selected this threshold to ensure that the areas in the vicinity of the electrodes were considered (laterally) and additionally, it led to include bottom elevations that have been reported as the original topography before the activities in the factory (approximately 110–115 m). In Fig. 3a we can note, overall, zones of larger resistivities towards the east and west end of the heap. Smaller resistivity values can be observed downhill of the heap (towards the west) at larger depths. In the chargeability model (Fig. 3b) we can observe shallow layers of large chargeability values and in particular a large zone which is distributed southeast- northwest with values up to 250 mV/V.

Based on the inverted models, the targeted sampling was composed of 22 samples collected at 8 different locations of the heap and at different depths of 1, 3 and 5 m (Fig. 1b and 3). Most of the samples were slags of similar color and structure except samples S04_5 and S05_3 which were mostly crushed bricks (see Figure C, Supp. Mat.).

The sampling survey targeted different zones of the inverted models, e.g., high and low values of resistivity and chargeability, combinations of large/low chargeability values and large/low resistivity values. Therefore, we assume that the collection of 22 samples taken at different positions (x, y, z) captures the variations of physical and chemical properties in the slag heap. In particular, note that the sharpest contrasts in the inverted models of resistivity and chargeability are in the shallowest zones. Then, we assume that the calibration of geophysical data

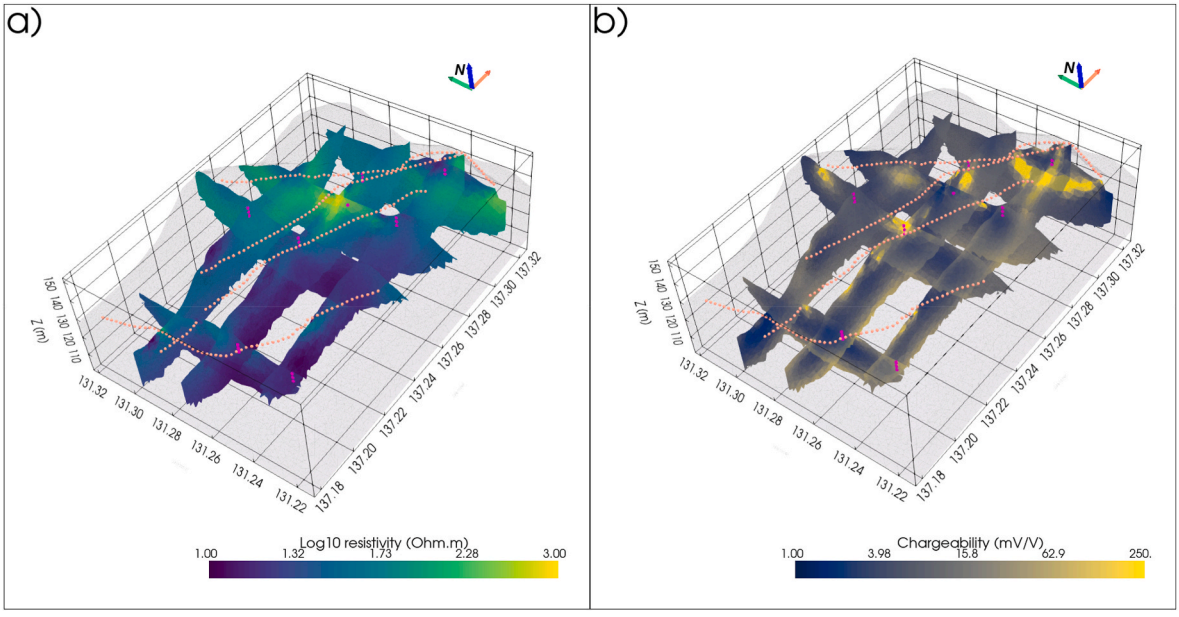

Fig. 3. 3D inverted models of a) resistivity and b) chargeability. Electrodes used in the acquisitions are shown in the heap ground surface as small salmon dots. Sampling location is indicated with the pink spheres.

with ground truth data observed at the first 5 m of the heap, can be extrapolated at larger depths, although the sensitivity and discriminating ability of ERT/IP decreases (Hermans and Irving, 2017; Isunza Manrique et al., 2023).

4.2. Laboratory measurements

4.2.1. ERT, IP and SIP data

Fig. 4a and b shows the laboratory measurements of resistivity and chargeability respectively. Most of the samples present similar ranges of resistivity (ρ lab) with slight variations with depth, except for samples S04 and S08, which present an increase and strong decrease of ρ with depth respectively. In terms of chargeability (m_{lab}), samples S06 and S02 present the largest values while sample S05 has $m_{lab} < 10$ mV/V. Overall no tendency is observed for the variations of chargeability with depth.

Fig. 4 also shows an overview of the SIP measurements through the magnitude of the resistivity $|\rho|$ (Fig. 4c), the real and imaginary components of the conductivity, σ' and σ'' (Fig. 4e and f), and the phase φ (Fig. 4d). We also included the SIP spectra of a water bearing column. Note that σ' increase with the frequency and σ'' displays a peak for most of the samples. In terms of the phase, we found that most of the samples are characterized by a peak of varying magnitudes, centered at around 1 Hz. This behavior has been reported before in iron slags (e.g., Florsch et al., 2011). S06 and S02 present the largest polarization magnitude through σ'' similar to the displayed largest chargeability.

4.2.2. Granulometry and XRF analysis

We compared the mass distribution of the samples at several size particles, from 65 μm to 40 mm, with the concentration of different elements (Fig. D, Supp. Mat.). On average, we observed that the mass of all samples was slightly higher in the particle sizes of 65 μm and from 10 to 40 mm. Note that in pyrometallurgical operations the slag forms megaliths that gradually break up in the ground because of erosion, which can explain the wide particle size distribution but similar chemical composition.

In terms of elements distribution, we noted that the calcium was

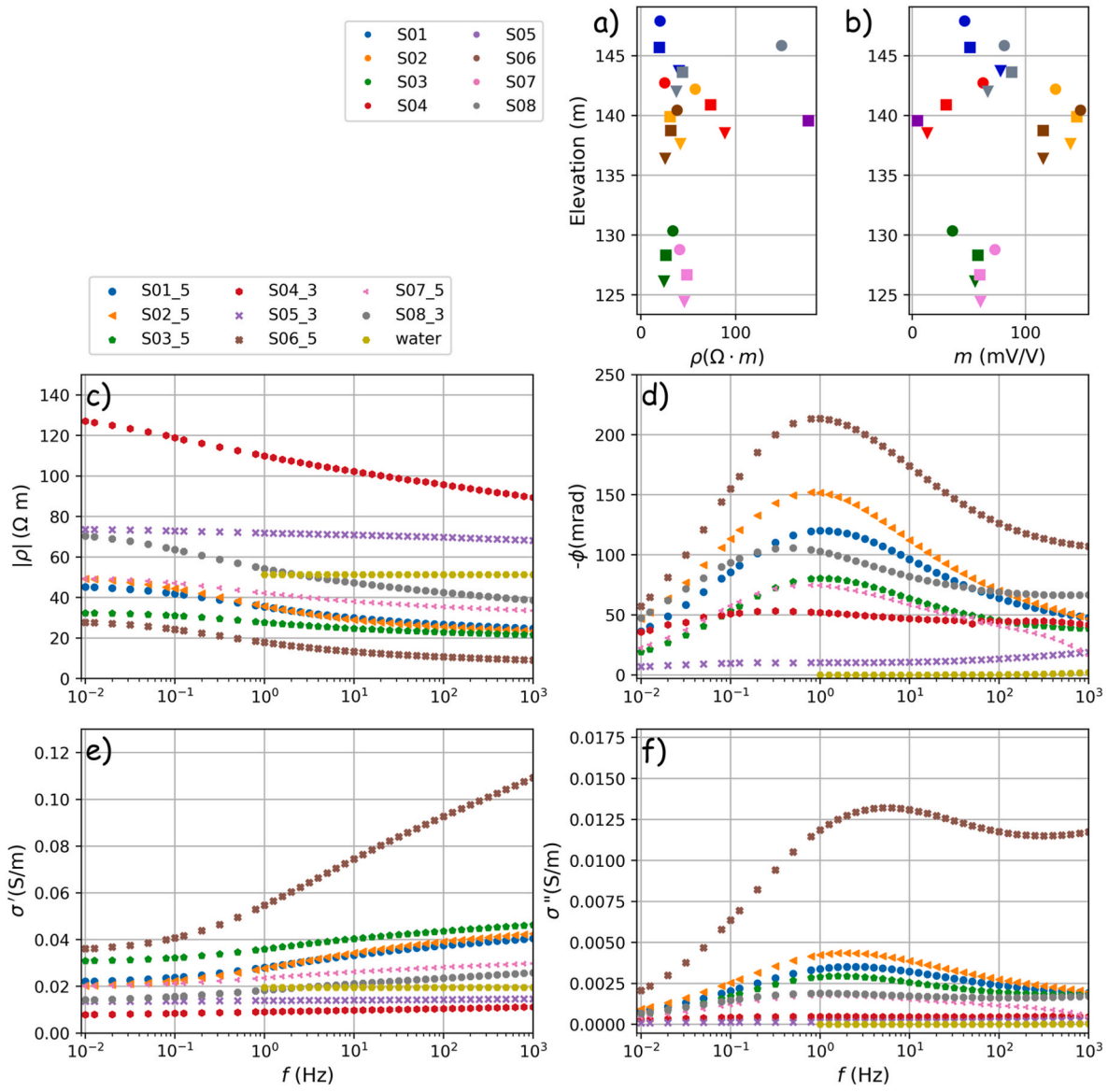

Fig. 4. Geophysical lab measurement of ERT, IP and SIP. First, we present the measurements of a) resistivity and b) chargeability. Each sample is plotted with their corresponding sampling depths at 1, 3 and 5 m, which are represented with a circle, square and triangle respectively. Then, an overview of SIP spectra is presented for some samples and a column filled with water. For clarity we only plot the spectra of eight samples, each at one location (x, y) and different depths. The image presents the c) magnitude of resistivity, d) phase, e) real component of complex conductivity and f) imaginary component of the complex conductivity.

distributed homogeneously in all the particle sizes for most of the subsamples although on average, the largest Ca concentration is observed in the particles of 10 mm. Secondly, the largest iron concentrations could be observed at the particle sizes >1 mm and the same pattern was observed for Mn. Lastly, only three samples presented larger concentrations of silicon, which was homogeneously distributed over all particle sizes.

4.3. Multivariate statistical analysis

4.3.1. Geochemical variables

Focusing on the elements with the largest weight concentrations (Si, Ca and Fe), we observed that Fe is largely correlated with Cr, V and Mn and negatively correlated with Al. Ca presents strong positive correlations with Sr and Mn, and negative correlations with Si, Ti and K. Si on the other hand, is largely correlated with Ti, K and Al and negatively correlated with Ca and Mn. This may indicate that the Fe group has a low concentration of Al and the Si group may have a low Ca content. Finally, note that some elements do not have pairwise strong correlations nor correlations with the elements above mentioned, these are Ni, Cu, S and Zn. The Pearson's correlation matrix between pairs of chemical elements concentrations is presented in Supp. material, Figure E.

4.3.2. Geochemical, lab-based and field-based geophysical variables

Fig. 5 includes correlations between 1) the chemical elements which are considered indicators of different types of slags, see section above, 2) resistivity and chargeability laboratory measurements indicated as ρ_{lab} and m_{lab}, see section 3.2.1, 3) the SIP measurements, specifically, the values of the real and imaginary components of the conductivity and the maximum magnitude of the phase observed at the polarization peak, as well as the frequency of the phase peak or critical frequency, i.e., σ'_{peak}, σ''_{peak}, $|\varphi_{peak}|$ and f_{peak} respectively, and 4) the values of resistivity ρ and chargeability m of the 3D inverted models (volume-averaged values centered at the sampling location). The yellow squares indicate the elements which are part of the critical raw material list of EU for 2023 (Grohol et al., 2023).

First, we can note that the measurements of resistivity in the lab (ρ_{lab}) and in the field (ρ) present strong correlations (>0.7) with the Si group previously identified. Then, the values of m_{lab} present large correlation with the Fe group with Fe (0.65), Mn (0.84), V (0.93) and Cr (0.82), while the values of chargeability from the field present a large correlation coefficient only with V. Regarding the SIP parameters, we did not observe correlations between σ'_{peak} nor σ''_{peak} and chemical elements, but large coefficients were observed between $|\varphi_{peak}|$ and the Fe group: Fe (0.75), Mn (0.83), V (0.93) and Cr (0.74). Lastly, there were no strong correlations between the SIP parameters and the concentrations of chemical elements in addition to those observed with m_{lab}.

As noted before, the values of ρ_{lab} and ρ present a strong positive correlation with the elements of the Si group (Si–Ti–K). Additionally, m_{lab} and m presented high correlations with the chemical elements of the group Fe, in particular m_{lab}, probably due to the sensed volume. The comparison between laboratory and field measurements, shows strong positive correlations (0.72) between ρ_{lab} - ρ and m_{lab} – m, which integrates the different sampled volume and the field and lab conditions. The discrepancy gives an idea of the scale and inversion effects on the validity of laboratory-derived petrophysical relationships (e.g., Benoit et al., 2019). In terms of the SIP parameters, note that there is a correlation of 0.82 between the imaginary and real components of the conductivity, which is a behavior that has been observed for several materials (Flores-Orozco et al., 2020). Although it is expected that the relaxation frequency is correlated with the particle size, this was not observed (results not presented here). Note that the samples do not have a predominant particle size (see section 3.2.2) which may explains the broad peaks in the phase spectra. Here, we included f_{peak} in the correlation matrix to study if variations in the composition of the slags could be discriminated through peak shifts in the phase spectra. However, no strong correlations were obtained with the geochemical variables.

There were two analyses that are not included in the correlation matrix of Fig. 5. First, we studied the correlations between the positions at which the samples were collected (x, y, z) and the geochemical and geophysical variables, however, no relations were found. This means that there are no preferential zones of similar composition within the heap (laterally nor vertically at least at the sampling resolution used here). Additionally, we fitted a double Cole-Cole model (Cole and Cole, 1941; Pelton et al., 1978) to the SIP phase spectra and studied the correlations between the spectral parameters (i.e., m, τ, ρ) and the geochemical variables to determine its ability to resolve composition variations. Nevertheless, no additional correlations were found, in addition to the complex conductivity parameters presented here.

In the following, we analyze the scatterplots of the ρ_{lab} - m_{lab} together with the concentration of some chemical elements with which the largest correlations were observed (i.e., Fe, Si and Mn) to identify groups

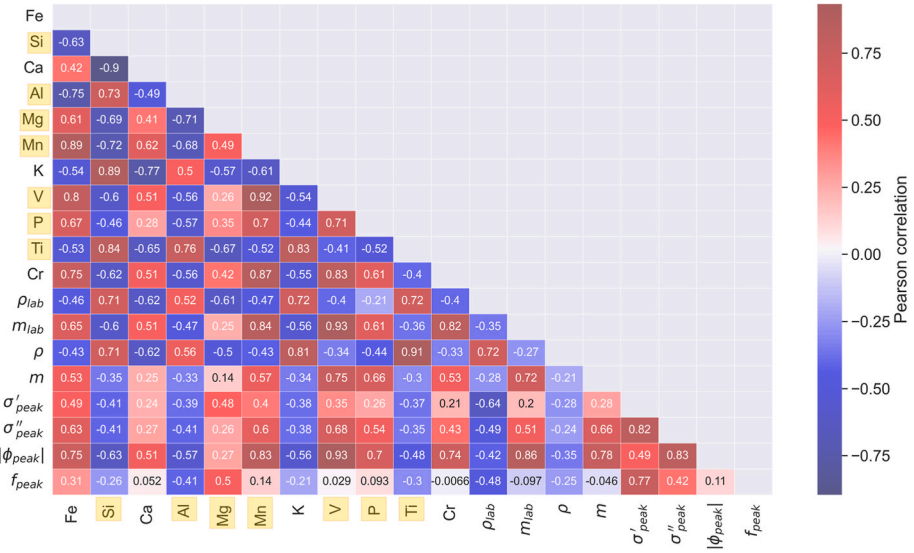

Fig. 5. Matrix of Pearson's correlation coefficients using some geochemical variables and geophysical variables. Yellow squares indicate the critical raw materials of the EU 2023.

or clusters of different composition. For comparison with the complex conductivities from SIP we will work with the conductivities σ_{lab} ($1/\rho_{lab}$). These scatterplots are displayed in Fig. 6a–c, with colorbars representing the average content of Mn, Fe and Si. We showed these elements due to the large correlations observed with the geophysical properties in Fig. 5 and their average concentration >1 wt%. First, we can note that the samples S04_5 and S05_3 can be identified with small chargeability values and small conductivities as well as large values of Si (likely to belong to the Si group mentioned in section 3.1.1). The remaining samples present intermediate to large concentrations of Fe and Mn and a small content of Si. Within this group, three clusters are observed. A cluster with the samples of largest chargeability and conductivity values (i.e., S02_3, S02_5, S06_1, S06_3, S06_5); another cluster with values $m_{lab} < 70$ mV/V and intermediate Fe–Mn content, i.e., S01_1, S01_3, S01_5, S03_1, S03_3, S03_5, S04_1, S04_3, S07_1, S07_3, S07_5, S08_5; lastly, a small cluster with $m_{lab} > 70$ mV/V, i.e., S02_1, S08_1, S08_3 (see Table 1). Nonetheless, the boundary of the last two groups is not clear as large concentrations of Fe–Mn can be observed for broad ranges of conductivities.

For comparison, we also analyzed the crossplots of σ''_{peak} vs σ'_{peak} and the average concentration of Mn and Fe (Fig. 6d–e). Similar to the ERT/IP measurements we can also observe that the samples attributed to Group 1 present the smallest values of σ''_{peak} and have low concentrations of Mn and Fe. Then, we can observe that the samples constituting groups 2, 3 and 4 are distributed along different linear relations $\sigma''_{peak} - \sigma'_{peak}$ as shown through the fittings of linear models displayed in Fig. 6d–e. We computed the coefficient of determination of these regressions and obtained $R^2 = 0.98$, $R^2 = 0.93$, and $R^2 = 0.85$ for the linear fittings in Group 2, 3 and 4 respectively. This supports the definition of the four groups and the attributed samples, as each of these linear models may represent different types of materials (through different phases, $\varphi \sim \sigma''/\sigma'$).

Afterwards, we carried out an unsupervised learning approach to group the samples from the time-domain lab measurements. Note that previous grouping was done integrating geochemical data while this approach only used geophysical parameters and can be obtained without samples. We applied a hierarchical clustering to previously standardized data, assuming four clusters and a single linkage as the metric criteria, i.e., minimizes distance between the closest observations of clusters pairs (Pedregosa et al., 2011). The results show that the clustering and the previous geophysical-geochemical grouping (Table 1) converge to similar group identification, which validates the proposed grouping. However, as the clustering minimizes the distance between the closest observations of pairs of groups, it can be sensitive to the initial model or the initial number of clusters (see Figure F, Supp. Mat.).

Table 1
Samples identified in each group from chemical analysis and geophysical lab measurements.

Group identifier	Samples	σ_{lab} (mS/m)	m_{lab} (mV/V)	Dominant concentration
Group 1	S04_5, S05_3	<20	<20	Si
Group 2	S02_3, S02_5, S06_1, S06_3, S06_5	>20	>100	Fe–Mn
Group 3	S01_1, S01_3, S01_5, S03_1, S03_3, S03_5, S04_1, S04_3, S07_1, S07_3, S07_5, S08_5	>14	<90 >20	Intermediate Fe–Mn
Group 4	S02_1, S08_1, S08_3	<25	>70	Intermediate Fe–Mn

4.3.3. *Principal component analysis (PCA)*

We applied PCA to the previously standardized geochemical and geophysical data shown in the correlation matrix of Fig. 5. The first three principal components (PC's) represent a variance of 55.35 %, 15 % and 10.22 % respectively, which add up to around 80 % of the total data variance.

First, we investigated how the samples (and clusters previously

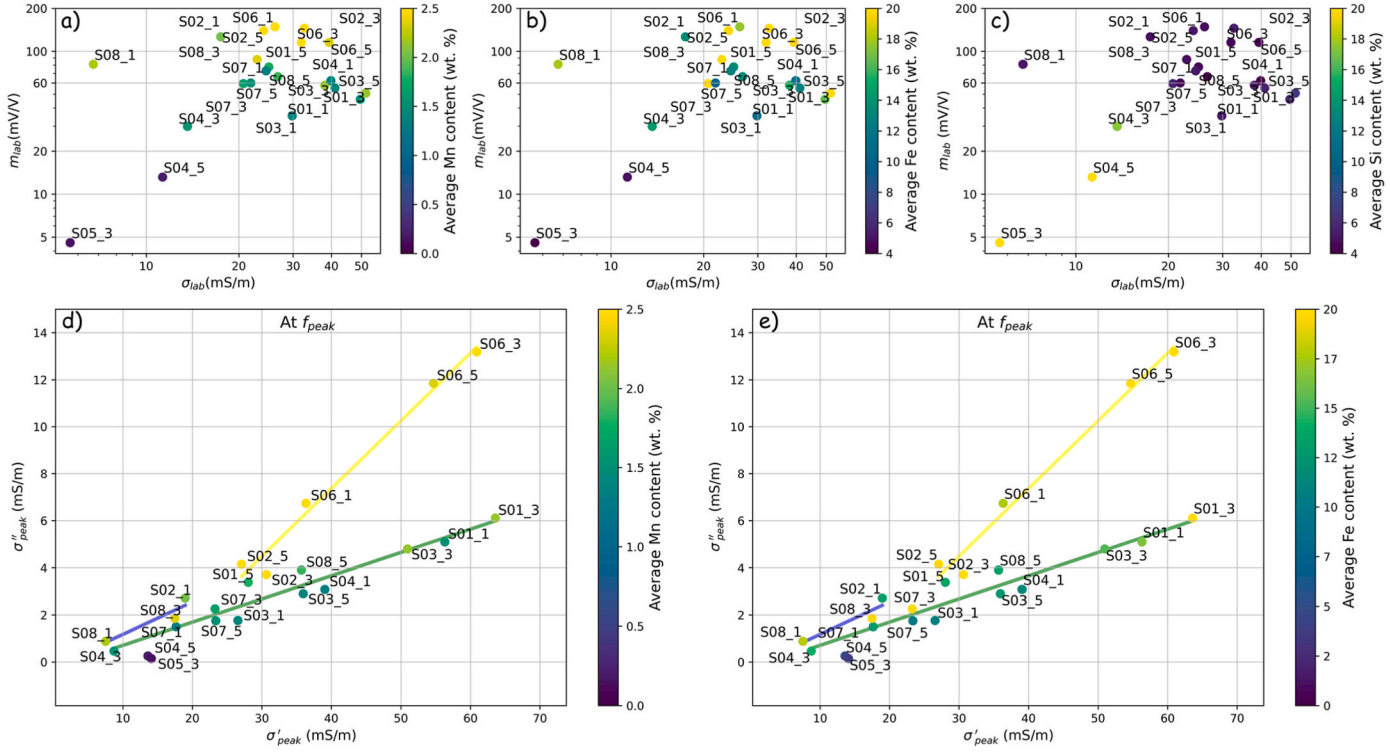

Fig. 6. Crossplots of the time-domain laboratory measurements of ERT- IP and complex conductivity at the frequency peak. (a–c) Chargeability vs conductivity ($1/\rho_{lab}$) with colorbars representing the average content of a) Mn, b) Fe and c) Si. (d–e) Real vs imaginary component of the conductivity with colorbars representing the average content of d) Mn and e) Fe. Lines represent the linear regressions with samples of Group 2 (yellow), Group 3 (green) and Group 4 in blue.

observed) were distributed in the PC's space (Fig. 7a–b). Focusing on the plot of PC2 vs PC1, we can again identify samples S04_5 and S05_3 (Group 1) as outliers which largely represent the data variance along PC1. Then, the samples with the largest values in the PC2 axis agree with the samples of largest chargeability and conductivity measurements (Group 2). In contrast, the samples with the smallest values in the PC2 axis constitute Group 3 and intermediate values in the PC2 axis correspond to Group 4. Overall, we can note that there are no overlaps of groups' samples.

Additionally, we computed the linear correlations between the PC's and the original variables using the correlation circles (Fig. 7c–e) for the first three PC's. Squared loadings are additionally presented in Supp. Mat. (Figure G). Note that PC1 presents strong correlations with most of the variables, e.g., positive large correlation with Si, Al, ρ_{lab}, ρ and negative correlations with Fe, Ca, Mn, m_{lab}, $|\varphi_{peak}|$. PC2 is predominantly related to the field resistivity and chargeability although the correlation coefficients with all variables are overall low. Lastly, PC3 is mainly related to the laboratory measurements of complex conductivity (σ''_{peak}; σ'_{peak}; f_{peak}) with which it is strongly correlated.

4.4. KDE's and probabilistic classification of field data

For visualization, we computed the 2D KDE's at a regular grid in the range of the inverted resistivity and chargeability models, based on the functions fitted with the volume-averaged field data (see Fig. 8a–d). The bandwidth of each group was estimated using Scott's rule. However, as the data distribution of Group 1 was oversmoothed, we decreased h from 0.56 to 0.3. On the other hand, the distribution of Group 3 was strongly influenced by the outliers, therefore, we slightly increased h from 0.19 to 0.3. This allowed to smooth the estimates increasing the covariance of the data distribution. In addition, these values of h led to classification results which are overall in line with the proportion of the groups 1–3 (or prior probabilities).

Then, we computed the 2D KDE's $f_{KDE}(\mathbf{y}|A_i)$ (see Eq. (1)) and the joint conditional probabilities $P(A_i|\mathbf{y})$ at the whole field data domain, for each group. The prior probability values $P(A_i)$ were estimated from the number of lab samples belonging to each group, these are 9%, 22 %, 54 % and 13 % for groups 1–4 respectively.

Fig. 8e–f also shows the classification of the field data, based on the largest joint conditional probabilities, as well as the volume-averaged field data (ρ, m) from which the 2D KDE's were built. In Fig. 8e the maximum transparencies represent the smallest probabilities of 33 % and in Fig. 8f we plot only the data with probability values larger than 50 %. Note that the smallest probabilities of classification are distributed in the boundaries of the groups.

4.5. Estimation of volumes

Fig. 9a–b shows the classification of the data along the same sections displayed before for the inverted models and the corresponding joint conditional probabilities with which each group or class was assigned. The maximum probability values are 1, 0.95, 1 and 0.85 for groups 1–4 while the minimum value with which the groups were selected was around 0.3.

Fig. 9c–f shows the volumes of each group. Comparing the probability weighted volumes (see Eq. (2)) with the volumes estimated without considering associated the probabilities, the estimated volumes with uncertainty ranges are reported in Table 2.

As indicated in Table 2, the volume of Group 1 represents the minority of the heap and it is mostly composed of Si, Ti and K (largely construction and demolition residues). The material of Group 2 is mostly concentrated on the east of the heap and scattered deposits distributed westwards. The material in this category presents the largest concentrations of Mn, Fe, V and Cr and it represents the most interesting volume for potential recovery. Then, the volume of Group 3 represents most of the slag heap material and it is distributed along the whole heap. Lastly, the intermediate volume of Group 4 is concentrated in the east of the heap and has scattered deposits westwards of the heap. As mentioned before, Groups 3 and 4 present very similar geophysical and

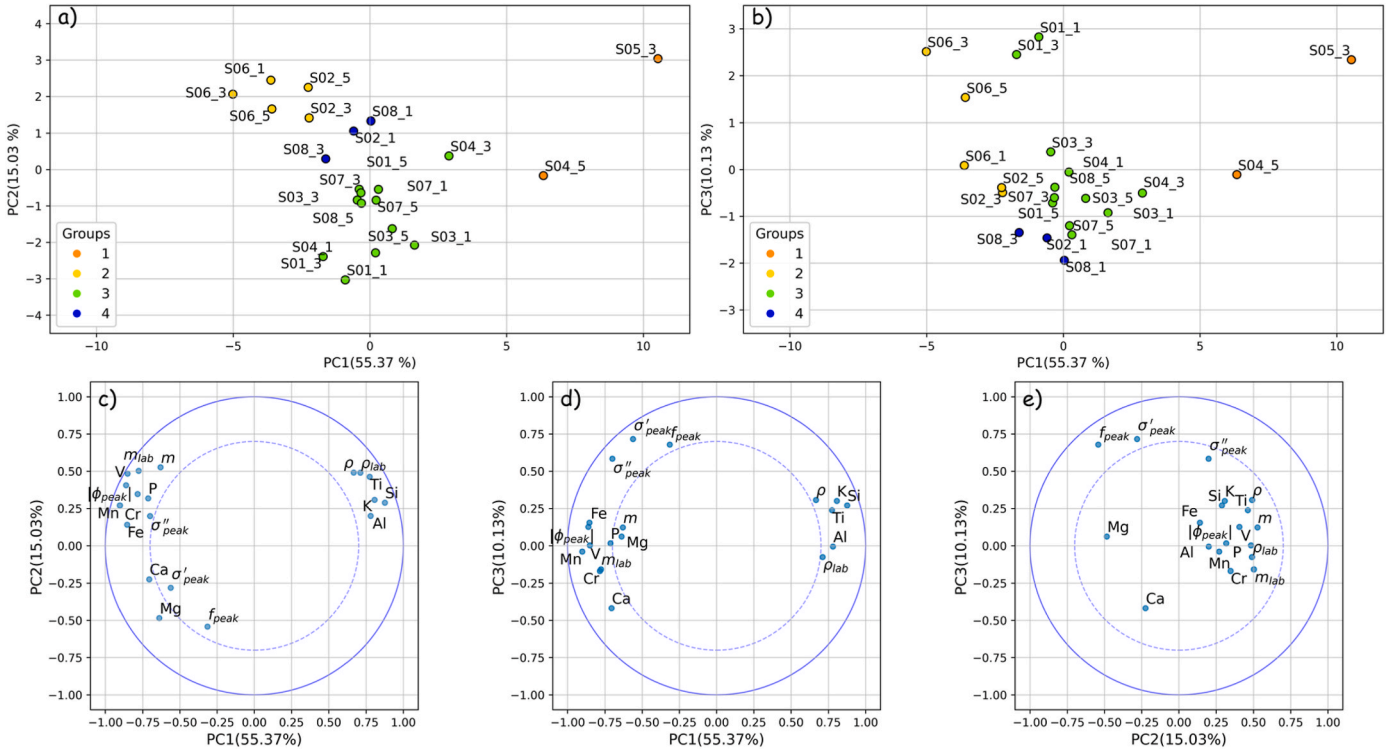

Fig. 7. (a–b) Samples represented in the axis of principal components: a) PC2 vs PC1 and b) PC3 vs PC1. (c–e) Correlation coefficients between the variables and c) PC2 vs PC1, d) PC3 vs PC1 and e) PC3 vs PC2. The radii of the circles represent a correlation coefficient of 0.7 and 1.

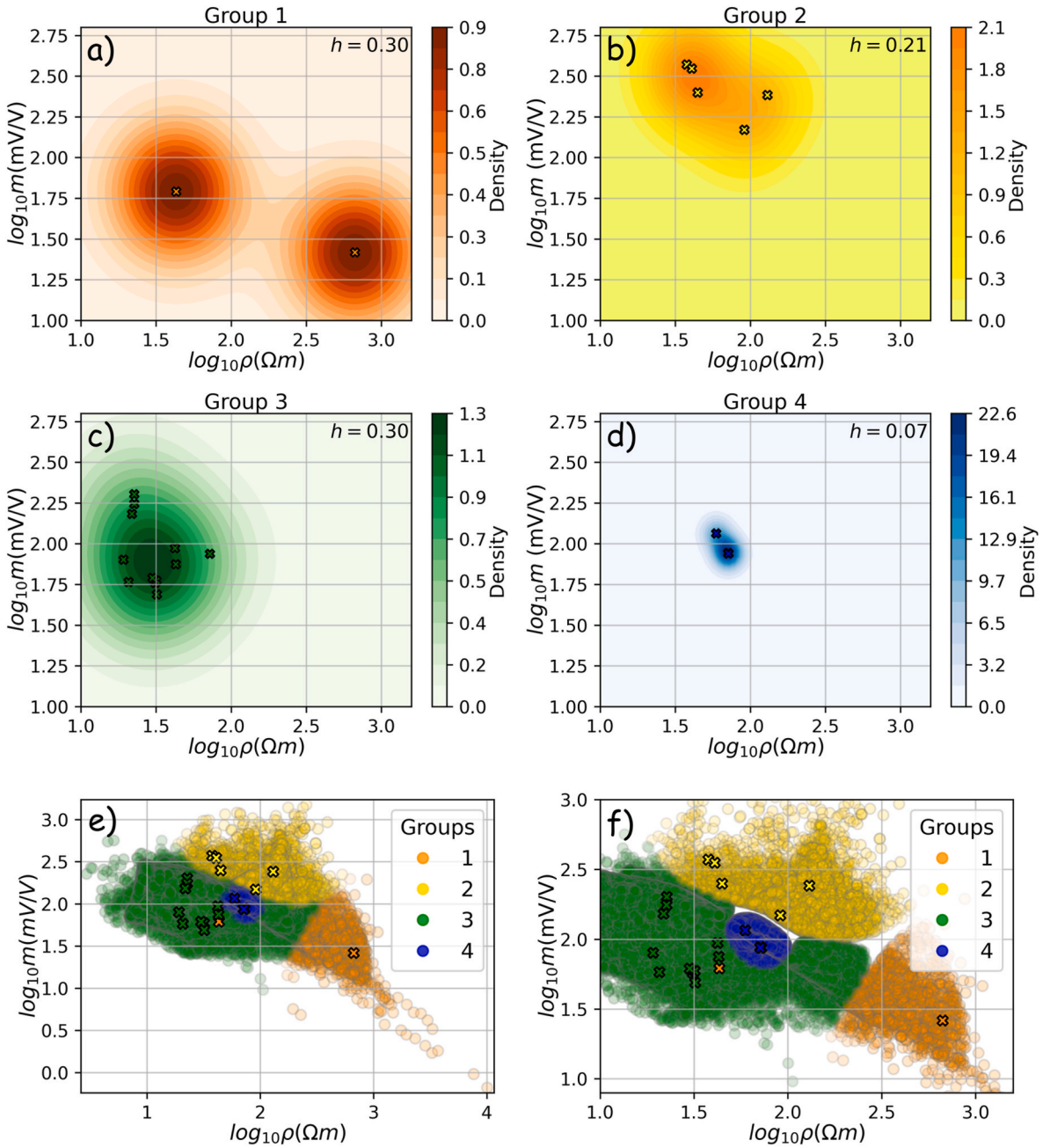

Fig. 8. (a–d) Joint probability density function using 2D KDE in a regular grid together with the volume-averaged field data collocated with the sampling for each group. (e–f) Classification of the field data. The lab measurements are displayed with crosses as well as their corresponding group color. The minimum joint probability is e) 33 % (maximum transparency). We also show in f) the classification considering only joint probability values larger than 50 %, with a special effect in boundaries of groups 2–4 and 1–2.

geochemical properties, yet the chargeability measured in samples of Group 4 are slightly larger than the ones in Group 3. Furthermore, the elements of Group 4 present in general, a larger concentration of Mn and possibly a larger concentration of quicklime (due to the strong correlation Mn–Ca). Due to the relatively low iron concentration in groups 3 and 4, these volumes can be potentially reused for road construction.

5. Discussion

The integrated methodology we followed seems suitable to quantitatively interpret geophysical field data using a probabilistic classification, according to a physics-based clustering from lab data. In the following, we describe the findings and limitations of the elements of this methodology.

For the measurements in the field, geoelectric methods have proved useful to derive insights into the composition of metallurgical deposits, even in intermediate-to-low concentrations of metals. As in practice, field acquisitions are tailored to be cost and time-efficient, ERT and time-domain IP represent suitable methods to be used in the field for a "rapid" investigation of metallurgical deposits (Martínez et al., 2019; Rey et al., 2021; Vásconez-Maza et al., 2021), in comparison with SIP field measurements which are still challenging. Electromagnetic and magnetic methods can also be used at this step. Nonetheless, deriving more accurate inverted models may require a previous data calibration for the electromagnetic method (Lavoué et al., 2010; Fraga et al., 2019) and in the case of magnetometry, both modelling and inversion can be

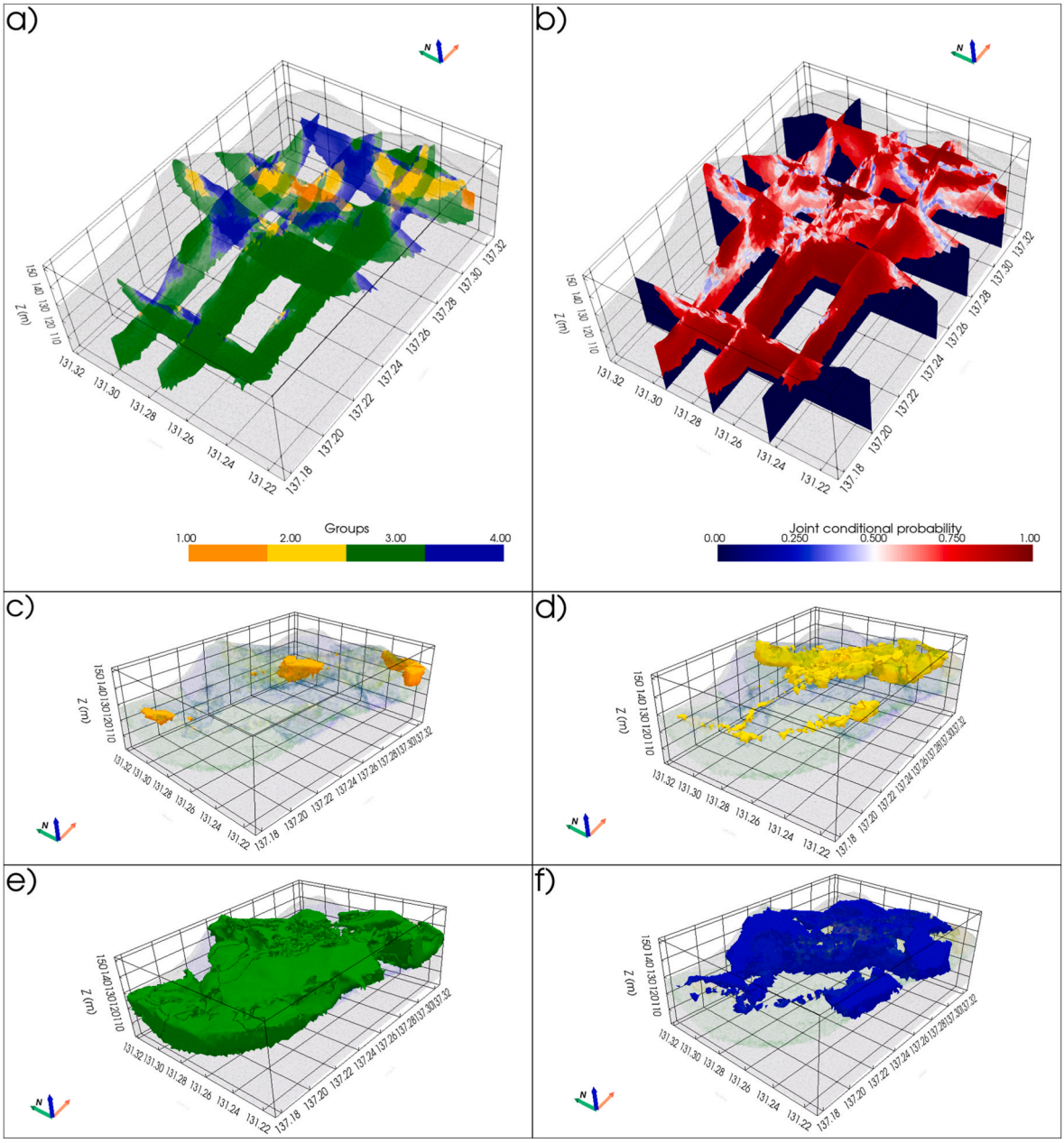

Fig. 9. a) Classification of the field data. Transparency along the sections represent the resulting probability values. b) Joint conditional probability sections. Both images integrate the sensitivity threshold ($>10^{-5.5}$). We also show the estimated volumes of c) group 1, d) group 2, e) group 3 and f) group 4.

Table 2
Estimated volumes for each group including uncertainty range, chemical composition and metallic concentration mostly based on Fe and Mn content.

Groups	Volume	Group composition	Metallic concentration
1	4.17×10^3 m^3 ± 12%	Si–Ti–K	Low
2	2.30×10^4 m^3 ± 21%	Fe–Mn–V–Cr	High
3	1.888×10^5 m^3 ± 12 %	Fe–Mn–V–Cr	Low-intermediate
4	59.4×10^3 m^3 ± 19 %	Fe–Mn–V–Cr	Intermediate- large

Note that these volumes exclude the cells of the inverted models where the sensitivity is less than $10^{-5.5}$, resulting in a total heap's volume of 275.4×10^3 m^3 ± 9%.

challenging in these anthropogenic environments (Vollprecht et al., 2019).

Second, the targeted sampling was designed to cover most of the lateral and vertical (shallow) variations of the inverted models. Therefore, here we assume that the 22 samples collected at different positions (x, y, z) represent ground truth data enough to capture the physical and chemical properties of the slag heap overall. Note that in the literature we can find sampling to be challenging and often samples are collected at surface, at several sites and/or at few locations (x, y) (Inzoli et al., 2016; Martin et al., 2021; Florsch et al., 2011). Few available samples may not represent the lateral nor vertical heterogeneity of the waste deposit, and consequently the resulting classification of the field data may only be valid in the vicinity of the samples positions.

Both geophysical laboratory measurements and geochemical analysis could show a variation in the samples. Overall, resistivity measurements were useful to identify different types of materials (slags and crushed bricks) and chargeability measurements could additionally resolve between different types of slags. SIP measurements support these findings with a varying phase magnitude as indicator of different types

of slags, which is not observed in the residues with crushed bricks. At this step, additional lab measurements can be carried out to better define the groups of samples, e.g., magnetic susceptibility. More detailed chemical analysis can be also conducted, based on which the field data can be ultimately interpreted.

Regarding the multivariate statistical analysis, first, we distinguished chemical elements of interest and inferred the composition of different types of slags through the correlation study of the elements' concentrations. Then, in the correlation study between geochemical and geophysical variables we identified the geophysical parameters that resolved variations of the chemical elements. We observed a linear relation between m_{lab} and the concentrations of Fe, Mn, V and Cr - similar as in Florsch et al. (2011)- and also strong correlations between ρ_{lab} and Si, K and Ti. In terms of SIP parameters, the amplitude of the phase at the frequency peak $|\varphi_{peak}|$ also presented a strong correlation with the Fe, Mn, V and Cr content. In the correlation matrix we also included the field measurements of resistivity and chargeability. While the resistivity values presented strong correlations with Si, Ca and Ti (as observed for the laboratory measurements) the chargeability was corelated only with vanadium. Furthermore, the correlations of $\rho_{\text{lab}} - \rho$ and $m_{\text{lab}} - m$ showed the scale difference derived from the comparison between "punctual" measurements directly from the samples and co-located volume-averaged data from inverted models. Although the correlation coefficients are relatively large (~0.7) and the field data may capture the variations observed in the laboratory measurements, the regularization effect of the inversion should still be considered. The identification of 4 groups was mostly based on different resistivity and chargeability ranges as well as the concentration of Fe, Mn and Si (Fig. 6a–c). A geophysics-based clustering leads to the same grouping as the geochemical-based one. This was supported first, with the complex conductivity at the relaxation frequency (i.e., different groups are associated with different phases, see Fig. 6d–e), a hierarchical clustering and PCA, where the groups are clearly distinguished in the PC2-PC1 space. Note that the aim of this step is to derive and support a physical-chemical-based grouping using 22 laboratory measurements. If several tens of samples are available, other approaches of unsupervised learning may be used, e.g., Whiteley et al. (2021).

Then, we modeled 2D KDE's using the volume-averaged field data collocated with the sampling for each previously identified group. Afterwards we estimated the KDE's at the whole domain of the inverted field data and computed joint conditional probabilities. The classification of the field data is strongly influenced by the selection of the bandwidth h in the definition of the KDE's. Yet, we observed that the two-step estimation of h represents a suitable alternative in presence of few data, i.e., the Scott's rule performs an automatic bandwidth estimation which can be tunned according to the level of noise we want to integrate in the model (which can be based on prior information). Furthermore, the selection of bandwidth also ensures that the classification of the data keeps the proportion of the prior probabilities established from the sampling. Lastly, the computation of joint conditional probabilities allowed to derive the uncertainty of the classification, which is of interest as for reserve classification.

Finally, the total volume estimated here is likely to represent a minimum threshold value. First, because the inverted models do not show the boundary between the slags and the host geology, whose natural level has been reported at around 115 m (but which could be deeper if natural soil was removed before the deposition of the slags). Secondly, because we included only the areas of the inverted models with a sensitivity larger than $10^{-5.5}$. Nonetheless, reporting the volumes with an uncertainty range (derived from computing volumes with and without consider associated probabilities) may lead to more accurate quantifications that can support remediation strategies especially in terms of resource recovery.

6. Conclusion

In this contribution we present an integrated methodology to quantitatively interpret geophysical field data in terms of chemical composition using a probabilistic classification. It ultimately allows to estimate the volumes of each class considering only parts of the inverted models that are sufficiently reliable (trough sensitivity) and integrating the uncertainty of the classification. We illustrate this methodology investigating a slag heap with residues from steel works and blast furnaces. Based on the statistical analysis of the geochemical and geophysical lab data, we identified 4 classes or groups from the 22 samples collected at different positions of the heap. Group 1 correspond to the inert waste with the largest concentration of Si, Ti and K; Group 2 represents the slags with the largest concentrations of Fe, Mn, Cr and V, which in turn represents the most interesting volume in terms of recovery; Group 3 and 4 refer to the materials with an intermediate Fe–Mn concentrations but the materials of Group 4 present a range of larger resistivities, which could be an indicator of a different type of slag. The estimated volumes of materials corresponding to groups 1–4 are respectively: 4.17×10^3 m^3 ± 12%, 2.30×10^4 m^3 ± 21%, 1.888×10^5 m^3 ± 12% and 59.4×10^3 m^3 ± 19%.

The methodology contains several elements that are crucial for the investigation of metallurgical residues, e.g., geophysical field acquisition, sampling, laboratory measurements, etc. It links laboratory and field measurements through a probabilistic classification that is based on the definition of multivariate KDE distributions (i.e., resistivity and chargeability) and allows to integrate uncertainties which can be translated to the estimation of volumes. Overall, we observe that defining elements of this methodology are: 1) a representative targeted sampling based on the results of the geophysical survey, to better infer prior probabilities and 2) the bandwidth selection for the definition of the 2D KDE's, where the examination of the geophysical volume-averaged field data distribution is considered. Note that the first element indicates that samples collected at few (x, y) locations and/or exclusively at surface may not reflect the heterogeneity nor the truth composition of the waste dump and may lead to misinterpretations of the field data. Furthermore, the selection of the bandwidth defines the KDE's distributions and therefore, it has a strong impact on the joint conditional probabilities and the classification. When few samples are considered for the computation of KDE, it may be challenging to set a bandwidth that integrates/excludes possible outliers, i.e., to define the weight that some samples will have on the estimation of the KDE distribution.

Lastly, the integrated methodology can be adapted according to the feature to investigate at the field scale. Laboratory measurements can include mineralogical analysis to interpret the field data in terms of mineral composition, or pedological descriptions, borehole-logs, back-scattered images, etc. Additionally, we found that reporting uncertainty ranges in the estimated volumes is useful information for stakeholders, managers and owners of these sites to make economically informed decisions while launching a resource-recovery and/or remediation project.

Credit author statement

Itzel Isunza Manrique: data acquisition, processing and interpretation, creation of figures, writing; Thomas Hermans: data interpretation, writing, conceptualization, supervision; David Caterina: data acquisition and processing, writing – review and editing; Damien Jougnot: writing – review and editing, supervision; Benoît Mignon and Antoine Masse: geochemical data acquisition and granulometry analysis in laboratory; Frédéric Nguyen: data interpretation, writing, conceptualization, supervision.

Declaration of competing interest

The authors declare that they have no known competing financial interests or personal relationships that could have appeared to influence the work reported in this paper.

Data availability

Codes and data necessary to reproduce the main results are available at: https://doi.org/10.5281/zenodo.10032420.

Acknowledgements

This work has been financed by the European Union's program of Interreg Norh-West Europe and the Wallon Region within the framework of the multidisciplinary project of NWE-REGENERATIS. We thank all project partners and group Duferco Wallonie.

Appendix A. Supplementary data

Supplementary data to this article can be found online at https://doi.org/10.1016/j.jenvman.2023.119366.

References

Asare, M.O., Afriyie, J.O., 2021. Ancient mining and metallurgy as the origin of Cu, Ag, Pb, Hg, and Zn contamination in soils: a review: water. Air, Soil Pollut. 232 (6), 240. https://doi.org/10.1007/s11270-021-05166-4.

Benoit, S., Ghysels, G., Gommers, K., Hermans, T., Nguyen, F., Huysmans, M., 2019. Characterization of spatially variable riverbed hydraulic conductivity using electrical resistivity tomography and induced polarization. Hydrogeol. J. 1 (27), 395–407. https://doi.org/10.1007/s10040-018-1862-7.

Canters, F., 1997. Evaluating the uncertainty of area estimates derived from fuzzy land-cover classification. Photogramm. Eng. Rem. Sens. 63 (4), 403–414.

Caterina, D., Beaujean, J., Robert, T., Nguyen, F., 2013. A comparison study of different image appraisal tools for electrical resistivity tomography. Near Surf. Geophys. 11 (6), 639–657. https://doi.org/10.3997/1873-0604.2013022.

Cole, K.S., Cole, R.H., 1941. Dispersion and absorption in dielectrics I. Alternating current characteristics. J. Chem. Phys. 9 (4), 341–351. https://doi.org/10.1063/1.1750906.

Dahlin, T., Zhou, B., 2006. Multiple-gradient array measurements for multichannel 2D resistivity imaging. Near Surf. Geophys. 4 (2), 113–123.

Das, I., Morlighem, M., Barnes, J., Gudmundsson, G.H., Goldberg, D., Dias dos Santos, T., 2023. In the quest of a parametric relation between ice sheet model inferred Weertman's Sliding-Law parameter and airborne radar-derived basal reflectivity underneath Thwaites glacier, Antarctica. Geophys. Res. Lett. 50 (10).

Dewar, N., Knight, R., 2020. Estimation of the top of the saturated zone from airborne electromagnetic data. Geophysics 85 (5), 63–76. https://doi.org/10.1190/geo2019-0539.1.

Dino, G.A., Cavallo, A., A. F, Piercarlo, R., Mancini, S., 2021. Raw materials supply: Kaolin and quartz from ore deposits and recycling activities. The example of the Monte Bracco area (Piedmont, Northern Italy). Resour. Pol. 74, 102413 https://doi.org/10.1016/j.resourpol.2021.102413.

Flores-Orozco, A., Gallistl, J., Steiner, M., Brandstätter, C., Fellner, J., 2020. Mapping biogeochemically active zones in landfills with induced polarization imaging: The Heferlbach landfill. Waste Manag. 107, 121–132. https://doi.org/10.1016/j.wasman.2020.04.001.

Florsch, N., Llubes, M., Téreygeol, F., Ghorbani, A., Roblet, P., 2011. Quantification of slag heap volumes and masses through the use of induced polarization: application to the Castel-Minier site. J. Archaeol. Sci. 38 (2), 438–451. https://doi.org/10.1016/j.jas.2010.09.027.

Florsch, N., Llubes, M., Téreygeol, F., 2012. Induced polarization 3D tomography of an archaeological direct reduction slag heap. Near Surf. Geophys. 10 (6), 567–574. https://doi.org/10.3997/1873-0604.2012042.

Fraga, Cavalcante, L. H, Schamper, C., Noël, C., Guérin, R., Rejiba, F., 2019. Geometrical characterization of urban fill by integrating the multi-receiver electromagnetic induction method and electrical resistivity tomography: a case study in Poitiers, France. Eur. J. Soil Sci. 70 (5), 1012–1024.

Grohol, M., Veeh, C., DG GROW, and European Commission, 2023. Study on the Critical Raw Materials for the EU 2023 Final Report. https://single-market-economy.ec.europa.eu/system/files/2023-03/Study%202023%20CRM%20Assessment.pdf.

Günther, T., Rücker, C., Spitzer, K., 2006. Three-dimensional modelling and inversion of DC resistivity data incorporating topography—II. Inversion. Geophys. J. Int. 166 (2), 506–517.

Hermans, T., Irving, J., 2017. Facies discrimination with ERT using a probabilistic methodology: effect of sensitivity and regularization. Near Surf. Geophys. 15, 13–25.

Inzoli, S., Giudici, M., Huisman, J.A., 2016. Estimation of sediment texture from spectral induced polarisation data using cluster and principal component analysis. Near Surf. Geophys. 14 (5), 433–447. https://doi.org/10.3997/1873-0604.2016033.

Isunza Manrique, I., David, C., Nguyen, F., Hermans, T., 2023. Quantitative interpretation of geoelectric inverted data with a robust probabilistic approach. Geophysics 88 (3), 73–88. https://doi.org/10.1190/geo2022-0133.1.

Izydorczyk, G., Mikula, K., Skrzypczak, D., Moustakas, K., Witek-Krowiak, A., Chojnacka, K., 2021. Potential environmental pollution from copper metallurgy and methods of management. Environ. Res. 197, 111050 https://doi.org/10.1016/j.envres.2021.111050.

Johansson, S., Lindskog, A., Fiandaca, G., Dahlin, T., 2020. Spectral induced polarization of limestones: time domain field data, frequency domain laboratory data and physicochemical rock properties. Geophys. J. Int. 220 (2), 928–950. https://doi.org/10.1093/gji/ggz504.

Lavoué, F., van der Krak, J., Rings, J., André, F., Moghadas, D., Huisman, J.A., Lambot, S., Weiherrnüller, L., Vanderborght, J., Vereecken, H., 2010. Electromagnetic induction calibration using apparent electrical conductivity modelling based on electrical resistivity tomography. Near Surf. Geophys. 8, 553–561.

Lévy, L., Maurya, P.K., Byrdina, S., Vandemeulebrouck, J., Sigmundsson, F., Árnason, K., Ricci, T., et al., 2019. Electrical resistivity tomography and time-domain induced polarization field investigations of geothermal areas at Krafla, Iceland: comparison to borehole and laboratory frequency-domain electrical observations. Geophys. J. Int. 218 (3), 1469–1489. https://doi.org/10.1093/gji/ggz240.

Lysdahl, A.K., Christensen, C.W., Pfaffhuber, A.A., Vöge, M., Andresen, L., Skurdal, G.H., Panzner, M., 2022. Integrated bedrock model combining airborne geophysics and sparse drillings based on an artificial neural network. Eng. Geol. 297, 106484 https://doi.org/10.1016/j.enggeo.2021.106484.

Machiels, L., Dinu, G., Onisei, L., Ku, Leuven, 2022. NEMO Closing Workshop to Present Key Results to Wide Group of Stakeholders.

Martin, T., Günther, T., Weller, A., Kuhn, K., 2021. Classification of slag material by spectral induced polarization laboratory and field measurements. J. Appl. Geophys. 194, 104439.

Martin, T., Kuhn, K., Günther, T., Kniess, R., 2020. Geophysical exploration of a historical stamp mill dump for the volume estimation of valuable residues. J. Environ. Eng. Geophys. 25 (2), 275–286. https://doi.org/10.2113/JEEG19-080.

Martínez Cortizas, A., López-Merino, L., Bindler, R., Mighall, T., Kylander, M.E., 2016. Early atmospheric metal pollution provides evidence for Chalcolithic/Bronze Age mining and metallurgy in southwestern Europe. Sci. Total Environ. 545, 398–406. https://doi.org/10.1016/j.scitotenv.2015.12.078.

Martínez, J., Rey, J., Sandoval, S., Hidalgo, M.C., Mendoza, R., 2019. Geophysical prospecting using ERT and IP techniques to locate galena veins. Rem. Sens. 11 (24), 2923. https://doi.org/10.3390/rs11242923.

Mendecki, M.J., Warchulski, R., Szczuka, M., Środek, D., Pierwoła, J., 2020. Geophysical and petrological studies of the former lead smelting waste dump in Sławków, Poland. J. Appl. Geophys. 179, 104080 https://doi.org/10.1016/j.jappgeo.2020.104080.

Moghadas, D., Badorreck, A., 2019. Machine learning to estimate soil moisture from geophysical measurements of electrical conductivity. Near Surf. Geophys. 17 (2), 181–195. https://doi.org/10.1002/nsg.12036.

Pedregosa, F., Varoquaux, G., Gramfort, A., Michel, V., Thirion, B., Grisel, O., Blondel, M., et al., 2011. Scikit-learn: machine learning in Python. J. Mach. Learn. Res. 12 (85), 2825–2830.

Pelton, W.H., Ward, S.H., Hallof, P.G., Sill, W.R., Nelson, P.H., 1978. Mineral discrimination and removal of inductive coupling with multifrequency IP. Geophysics 43 (3), 588–609. https://doi.org/10.1190/1.1440839.

Qi, Y., A, Soueid, A., Revil, A., Ghorbani, A., Abdulsamad, F., Florsch, N., Bonnenfant, J., 2018. Induced polarization response of porous media with metallic particles — Part 7: Detection and quantification of buried slag heaps. Geophysics 83 (5), E277–E291. https://doi.org/10.1190/geo2017-0760.1.

Reback, J., McKinney, W., Van Den Bossche, J., Augspurger, T., Cloud, P., Klein, A., Hawkins, S., Roeschke, M., Tratner, J., et al., 2020. Pandas-Dev/Pandas: Pandas 1.0.5. Zenodo.

Revil, A., Vaudelet, P., Su, Z., Chen, R., 2022. Induced polarization as a tool to assess mineral deposits: a review. Minerals 12 (571). https://doi.org/10.3390/min12050571.

Rey, J., Martínez, J., Hidalgo, M.C., Mendoza, R., Sandoval, S., 2021. Assessment of tailings ponds by a combination of electrical (ERT and IP) and hydrochemical techniques (Linares, Southern Spain). Mine Water Environ. 40 (1), 298–307. https://doi.org/10.1007/s10230-020-00709-3.

Scott, D.W., 1992. Multivariate Density Estimation: Theory, Practice, and Visualization. John Wiley & Sons.

Sethurajan, M., van Hullebusch, E.D., Nancharaiah, Y.V., 2018. Biotechnology in the management and resource recovery from metal bearing solid wastes: recent advances. J. Environ. Manag. 211, 138–153. https://doi.org/10.1016/j.jenvman.2018.01.035.

Slater, L., Binley, A.M., Daily, W., Johnson, R., 2000. Cross-hole electrical imaging of a controlled saline tracer injection. J. Appl. Geophys. 44 (2), 85–102.

Sullivan, C., Kaszynski, A., 2019. PyVista: 3D plotting and mesh analysis through a streamlined interface for the Visualization Toolkit (VTK). J. Open Source Softw. 4 (37), 1450.

Van De Vijver, E., Isunza Manrique, I., Bobe, C., Caterina, D., Hermans, T., Wille, E., Nguyen, F., 2021. Geophysics in Support of Dynamic Landfill Management: Moving beyond the Challenges: First International Meeting for Applied Geoscience & Energy. https://doi.org/10.1190/segam2021-3594435.1. SEG/AAPG/SEPM, Expanded Abstracts.

Van Hoorde, M., Hermans, T., Dumont, G., Nguyen, F., 2017. 3D electrical resistivity tomography of karstified formations using cross-line measurements. Eng. Geol. 220, 123–132. https://doi.org/10.1016/j.enggeo.2017.01.028.

Vareda, J.P., Valente, A.J.M., Durães, L., 2019. Assessment of heavy metal pollution from anthropogenic activities and remediation strategies: a review. J. Environ. Manag. 246, 101–118. https://doi.org/10.1016/j.jenvman.2019.05.126.

Vásconez-Maza, M.D., Martínez-Segura, M.A., Bueso, M.C., Faz, Á., García-Nieto, M. C.a, Gabarrón, M., Acosta, J.A., 2019. Predicting spatial distribution of heavy metals in an abandoned phosphogypsum pond combining geochemistry, electrical resistivity tomography and statistical methods. J. Hazard Mater. 374, 392–400. https://doi.org/10.1016/j.jhazmat.2019.04.045.

Vásconez-Maza, M.D., Bueso, M.C., Faz, A., Acosta, J.A., Martínez-Segura, M.A., 2021. Assessing the behaviour of heavy metals in abandoned phosphogypsum deposits combining electrical resistivity tomography and multivariate analysis. J. Environ. Manag. 278, 111517 https://doi.org/10.1016/j.jenvman.2020.111517.

Virtanen, P., Gommers, R., Oliphant, T.E., Haberland, M., Reddy, T., Cournapeau, D., Burovski, E., et al., 2020. SciPy 1.0: Fundamental algorithms for scientific computing in Python. Nat. Methods 17 (3), 261–272. https://doi.org/10.1038/s41592-019-0686-2.

Vollprecht, D., Bobe, C., Stiegler, R., Van De Vijver, E., Wolfsberger, T., Küppers, B., Scholger, R., 2019. Relating magnetic properties of municipal solid waste constituents to iron content: implications for enhanced landfill mining. Detritus 8, 31–46.

Whiteley, J.S., Watlet, A., Uhlemann, S., Wilkinson, P., Boyd, J.P., Jordan, C., Kendall, J. M., Chambers, J.E., 2021. Rapid characterisation of landslide heterogeneity using unsupervised classification of electrical resistivity and seismic refraction surveys. Eng. Geol. 290, 106189 https://doi.org/10.1016/j.enggeo.2021.106189.

Zhang, Y., Wei, L., Lu, Q., Zhong, Y., Yuan, Z., Wang, Z., Li, Z., Y, Yang, Y., 2023. Mapping soil available copper content in the mine tailings pond with combined simulated annealing deep neural network and UAV hyperspectral images. Environ. Pollut. 320, 120962.

Žibret, G., Bruno, L., Mendez, A.-M., Cormio, C., Sinnett, D., Cleall, P., Szabó, K., Carvalho, M.T., 2020. National mineral waste databases as an information source for assessing material recovery potential from mine waste, tailings and metallurgical waste. Minerals 10 (5), 446. https://doi.org/10.3390/min10050446.

Zimmermann, E., Kemna, A., Berwix, J., Glaas, W., Münch, H.M., Huisman, J.A., 2008. A high-accuracy impedance spectrometer for measuring sediments with low polarizability. Meas. Sci. Technol. 19 https://doi.org/10.1088/0957-0233/19/10/105603.